

1 Thermal Annealing of Implanted ²⁵²Cf Fission-Tracks in Monazite

2

3

Sean Jones, Andrew Gleadow, Barry Kohn

4

5

School of Earth Sciences, University of Melbourne, Victoria 3010, Australia

6

7 **Correspondence:** Sean Jones (seanj1@student.unimelb.edu.au)

8

9 **Abstract**

10 A series of isochronal heating experiments were performed to constrain monazite fission-track thermal annealing properties. ²⁵²Cf fission-tracks were implanted into monazite crystals
11 from the Devonian Harcourt Granodiorite (Victoria, Australia) on polished surfaces oriented
12 parallel to (100) pinacoidal faces and perpendicular to crystallographic c-axis. Tracks were
13 annealed over 1, 10, 100 and 1000 hour schedules at temperatures between 30°C and 400°C.
14 Track lengths were measured on captured digital image stacks, and then converted to
15 calculated mean lengths of equivalent confined fission tracks which progressively decreased
16 with increasing temperature and time. Annealing is anisotropic, with tracks on surfaces
17 perpendicular to the crystallographic c-axis consistently annealing faster than those parallel
18 to the (100) face. To investigate how the mean track lengths decreased as a function of
19 annealing time and temperature, one parallel and two fanning models were fitted to the
20 empirical dataset. The temperature limits of the monazite partial annealing zone (MPAZ)
21 were defined as length reductions to 0.95 (lowest) and 0.5 (highest) for this study.
22 Extrapolation of the laboratory experiments to geological timescales indicates that for a
23 heating duration of 10⁷ years, estimated temperature ranges of the MPAZ are -44 to 101°C
24 for the parallel model and -71 to 143°C (both ± 6 ± 21°C, 2 standard errors) for the best fitting
25 linear fanning model ($T_0 = \infty$). If a monazite fission-track closure temperature is approximated
26 as the mid-point of the MPAZ, these results, for tracks with similar mass and energy
27 distributions to those involved in spontaneous fission of ²³⁸U, are consistent with previously
28 estimated closure temperatures (calculated from substantially higher energy particles) of
29 <50°C and perhaps not much above ambient surface temperatures. Based on our findings we
30 estimate that this closure temperature (T_c) for fission tracks in monazite ranges between ~45
31

Deleted: (100) prismatic faces

Deleted: on surfaces

Deleted: parallel to c

Deleted: -

36 and 25°C over geological timescales of $10^6 - 10^7$ years making this system potentially useful
37 as an ultra-low temperature thermochronometer.

38

39 **1. Introduction**

40 Fission track thermochronology is an analytical technique used to reconstruct the low-
41 temperature thermal history of rocks over geological time. Fission tracks form from the
42 spontaneous nuclear fission of ^{238}U , resulting in the accumulation of narrow damage trails in
43 uranium-bearing minerals such as apatite and zircon. The time since the fission tracks began
44 to accumulate may be calculated by measuring the spontaneous track density and uranium
45 concentration. If the host rock experienced elevated temperatures, the fission tracks that
46 have formed up to that point will progressively anneal and eventually disappear. Thermal
47 diffusion drives the annealing process, with the reduction in fission track density and confined
48 track length being a function of heating time and temperature in the host rock. From the
49 apparent age and track length distribution a quantitative analysis of the thermal history of
50 the host rock can be achieved. For fundamentals of the fission track technique, including
51 methodology and applications see Wagner and Van den Haute (1992) and Malusa and
52 Fitzgerald (2019).

53

54 The occurrence of monazite as an accessory mineral, along with the presence of significant
55 uranium (U) and thorium (Th) incorporated in its crystal lattice make it a useful mineral for
56 isotopic and chemical dating (e.g. Badr et al., 2010; Cenki-Tok et al., 2016; Tickyj et al., 2004).
57 In monazite, studies have mostly focused on the U-Th-Pb and (U-Th)/He systems but only
58 limited research has been carried out into the potential of the fission track system, mainly
59 due to technological limitations. Conventional fission track dating relies on thermal neutron
60 irradiation of samples to obtain an estimate of ^{238}U content via the formation of ^{235}U fission
61 tracks, usually captured in an adjacent external solid-state track detector such as mica. This
62 approach, however, has hindered the development of monazite fission track dating for a
63 number of reasons. Monazite is highly unsuitable for irradiation due to massive self-shielding
64 by thermal neutron capture from gadolinium (Gd), which may reach abundances in excess of
65 2 wt%. Gd has an extremely high thermal neutron capture cross-section of 48,890 barns,
66 averaged over its constituent isotopes, compared to 580 barns for ^{235}U fission (Gleadow et
67 al., 2004; Weise et al., 2009). An even more serious issue is that neutron capture by Gd

68 induces substantial nuclear heating in monazite during irradiation, which may be sufficient to
69 melt the grains and would certainly anneal any fission tracks produced.

70

71 These factors have also ruled out conventional annealing studies dependent on neutron-
72 induced ^{235}U fission tracks to assess the geological stability of fission tracks in this mineral.
73 Alternative thermal annealing experiments have been developed using implanted heavy ion
74 tracks (e.g. Weise et al., 2009; Ure, 2010), in place of ^{235}U induced fission tracks. These
75 methods, in combination with the use of Laser Ablation ICP Mass Spectrometry (LA-ICPMS)
76 or Electron Probe Microanalysis (EPMA) for determining U concentrations on individual
77 grains, provide alternatives to the traditional neutron-irradiation approach, thus allowing the
78 potential of monazite fission track dating to be assessed.

79

80 The first published study of fission track dating in monazite was by Shukoljukov and Komarov
81 (1970), who reported very young ages for two monazite samples from Kazakhstan. The
82 unexpectedly young results obtained were the first to suggest that fission tracks in monazite
83 anneal at relatively low temperatures (Shukoljukov and Komarov, 1970). Since this study, the
84 majority of reported monazite fission track studies have been in conference abstracts (e.g.
85 Fayon, 2011, Gleadow et al., 2004, and Shipley and Fayon, 2006). Gleadow et al. (2004)
86 reported preliminary results on several monazite samples revealing fission track ages
87 considerably younger than corresponding apatite fission track ages, further suggesting that
88 monazite fission tracks anneal at lower temperatures. This finding was later confirmed by
89 Shipley and Fayon (2006), who also suggested that annealing rates may vary as a function of
90 uranium concentration.

91

92 A comprehensive annealing study using 300MeV ^{86}Kr heavy ion tracks in monazite was
93 published by Weise et al. (2009). Three isochronal annealing sequences were carried out over
94 schedules of 1, 20 and 100 hr/s on crystals cut parallel to the (100) face. Adapting simplified
95 apatite annealing models and extrapolating the results to geological timescales they
96 estimated a closure temperature that "is in all likelihood $<50^\circ\text{C}$ and perhaps not much above
97 ambient".

98

99 Ure (2010) carried out further thermal annealing experiments on monazite based on
100 implanted ^{252}Cf fission tracks. These were carried out on grains mounted parallel to (100)
101 pinacoidal faces and perpendicular to the crystallographic c-axis, with each orientation
102 annealed for 20 minutes and 1 hour at various temperatures. The results showed that on
103 these short laboratory time scales, ^{252}Cf tracks in monazite annealed at lower temperatures
104 when compared to parallel experiments on Durango apatite. Further, it was concluded that
105 monazite exhibits similar anisotropic annealing properties to apatite in that tracks anneal
106 faster perpendicular to the c-axis compared to the c-axis parallel direction. All of these studies
107 have suggested that fission tracks in monazite have significant potential as a new ultra-low
108 temperature thermochronometer, but that further work is required to quantify the annealing
109 kinetics.

110

111 Several studies have used heavy ion tracks as proxies for fission track annealing studies in
112 other minerals. Green et al. (1986) annealed 220-MeV Ni ion tracks in apatite to further
113 confirm that gaps in the etchability of highly annealed tracks delay the progress of the etchant
114 along the track length. Sandhu et al., (1990) implanted heavy ion tracks of various energies
115 (1.67 GeV Nb, 3.54 GeV Pb and 2.38 GeV U) in mica, apatite and zircon, and concluded that
116 the activation energies for annealing the different energy ion tracks were identical in the
117 same mineral. Furthermore, they found that in the same mineral, the activation energies for
118 annealing of tracks formed by ^{252}Cf fission fragments were also identical to those from the
119 heavy ion tracks. These studies have shown that the minimum energy required to initiate
120 annealing is largely independent of the nature and energy of the ion source and rather is a
121 property of the detector mineral (Sandhu et al., 1990). Because the mass and energy
122 distributions of both light and heavy fission fragments from ^{252}Cf are similar to those
123 produced by spontaneous fission of ^{238}U , the annealing properties of fission tracks from either
124 source in monazite should be similar (Fleischer et al., 1975).

125

126 In this study, implanted ^{252}Cf fission tracks are used to constrain the thermal annealing
127 properties of monazite using a modified etching protocol (Jones et al., 2019). The new
128 annealing experiments cover a wider time-temperature range than previously reported.
129 Three alternative kinetic models are then developed that describe the reduction of fission
130 track lengths as functions of time and temperature. Extrapolation of these models then allows

Deleted: A

132 estimates to be made of the temperature range over which fission-track annealing occurs on
133 geological timescales.

134

135 **2. Experimental methods**

136 Monazite crystals used in the thermal annealing experiments were separated from the Late
137 Devonian Harcourt Granodiorite (Victoria, Australia). This is a high-K, calc-alkaline granite
138 dated by zircon U-Pb and $^{40}\text{Ar}/^{39}\text{Ar}$ geochronology to ~ 370 Ma (Clemens, 2018). Euhedral
139 monazite crystals range from $\sim 100 - 250$ μm in length and are classified as Ce dominant (see
140 Table 1).

141

142 **Table 1.** Average electron microprobe analyses of Harcourt Granodiorite monazite grains

Element	Mean Wt.%
SiO ₂	1.63 ± 0.04
P ₂ O ₅	27.37 ± 0.15
CaO	0.45 ± 0.02
Y ₂ O ₃	2.39 ± 0.05
La ₂ O ₃	14.13 ± 0.17
Ce ₂ O ₃	28.54 ± 0.26
Pr ₂ O ₃	4.45 ± 0.11
Nd ₂ O ₃	10.61 ± 0.13
Sm ₂ O ₃	1.80 ± 0.08
Gd ₂ O ₃	1.34 ± 0.08
ThO ₂	6.31 ± 0.11
UO ₂	0.50 ± 0.04
Sum Ox%	99.52

Measurements ($\pm 2\sigma$ error) on 81 grains made with a Cameca SX50 electron microprobe using a 10 μm beam width, 50 KeV beam current, 25 KV accelerating voltage and take off angle of 40°.

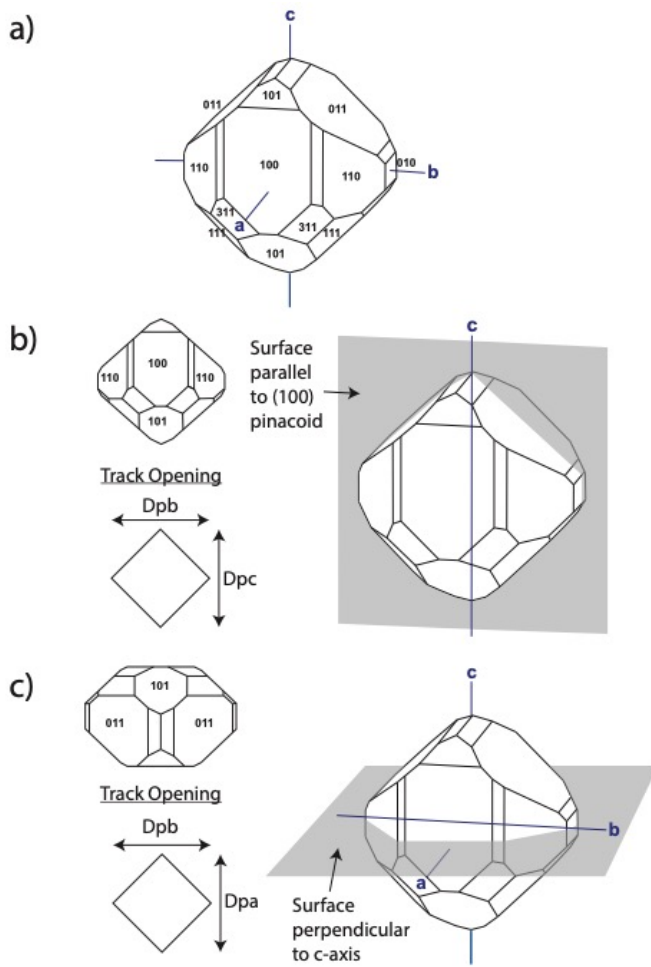
143

144

145 ^{252}Cf fission track implantation, measurements and equivalent confined fission track
146 calculations in this study essentially followed the procedure of Ure (2010). Fifty-five monazite
147 crystals per sample were pre-annealed (400°C for 8 hours) and attached to double-sided tape
148 on a Teflon block. Then using tweezers under a stereoscopic microscope, grains were carefully
149 oriented parallel (//) to (100) pinacoidal faces and perpendicular (\perp) to the crystallographic
150 c-axis (Figure 1), followed by mounting in cold setting *Struers* Epofix epoxy. For each annealing
151 experiment, two sample mounts were made, one with grains orientated parallel to the (100)
152 face and another to the c-axis. Each sample mount was then pre-ground using a *Struers* MD-
153 Piano 1200 grinding disc and final polishing with 6, 3, 1 and 0.25 μm diamond pastes. Polished
154 grain mounts were then exposed to collimated fission fragments approximately 2 cm from a

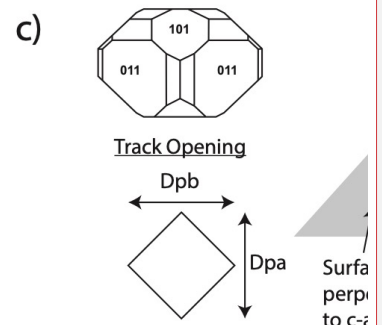
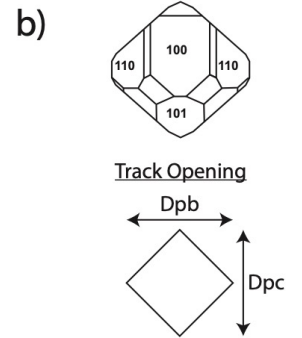
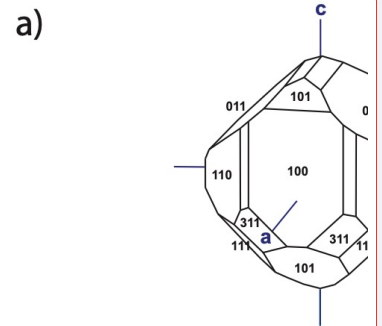
Deleted: perpendicular

156 thin 4mm diameter ^{252}Cf source under vacuum for 7 hours to implant a density of $\sim 5 \times 10^6$
 157 tracks/cm². Tracks were implanted at an angle of approximately 30° to the polished surface
 158 which had been shown to be optimal for measurement in previous experiments (Ure, 2010).
 159 Although the grains were mounted in precise orientations, both surfaces had limited control
 160 on the precise azimuth of the collimated tracks.



162
 163 **Figure 1.** (a) Typical monazite crystal with Miller Indices and crystallographic axes. (b) Crystal plane for tracks
 164 implanted on surfaces parallel to the (100) pinacoid face (i.e., parallel to the b- and c-axes). The shape of the

Deleted:



Deleted:

Formatted: Font: 10 pt

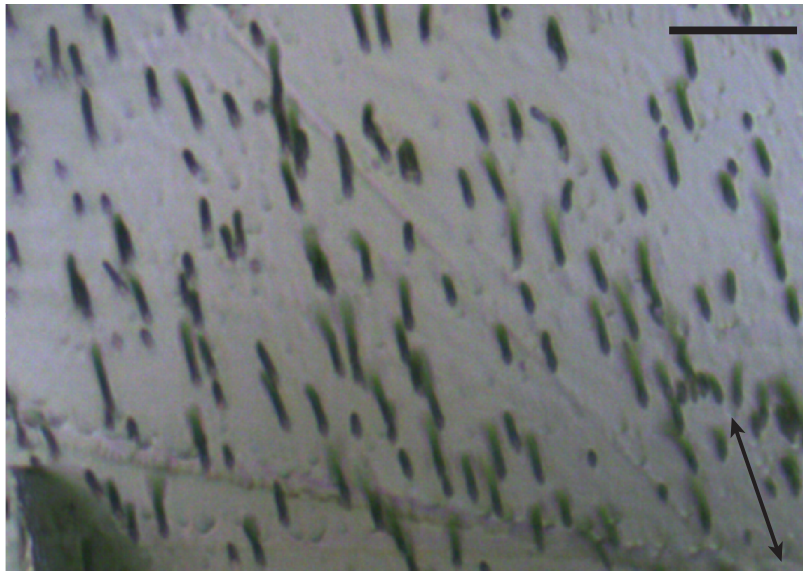
Deleted: crystallographic c-axis

Formatted: Font: 10 pt

168 track opening on the etched surface is a rhombus. Dpb represents diameter of etch pit parallel to b-axis and Dpc
169 is defined as the diameter of etch pit parallel to c-axis, equivalent to the parameters Dper and Dpar respectively
170 in uniaxial minerals such as apatite. (c) Crystal plane for tracks implanted perpendicular to c-axis. Track etch pits
171 also tend to be diamond in shape. Dpa represents diameter of track opening parallel to a-axis. Models from
172 Mindat.org.

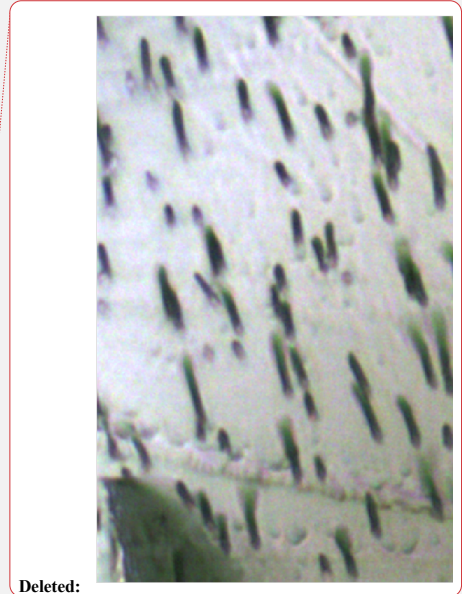
173
174 Following track implantation, grains were removed from the mount by dissolving the epoxy
175 mount in commercial paint-stripper. The loose grains were then annealed in aluminum tubes
176 in a *Ratek Digital Dry Block Heater* over 1-, 10-, 100- and 1000-hour schedules at
177 temperatures between 30°C → 400°C. The block heater was covered by a ceramic foam block
178 for insulation through which a probe could be inserted to monitor temperatures.
179 Temperature uncertainty is estimated to be ± 2°C. Once each annealing experiment was
180 completed, the grains were removed from the block heater and re-mounted, polished face
181 down, on double-sided tape before re-embedding in cold setting *Epofix* epoxy. Etching of each
182 sample mount was then performed using 6M HCl for 75 minutes at 90°C (Jones et al., 2019).
183 An example of well-etched ²⁵²Cf fission tracks in this monazite is shown in Figure 2.

184



185

Deleted: -



Deleted:

188 **Figure 2.** Implanted and well-etched ²⁵²Cf fission tracks in Harcourt Granodiorite monazite. Tracks are implanted
189 on surfaces parallel to the (100) pinacoid. Arrow indicates direction of the c-axis. Enlarged image taken with a
190 100x dry objective, scale bar is 10 μm.

191
192 Digital images of all monazite grains in each mount were captured in reflected and
193 transmitted light using a 100x dry objective on a Zeiss Axio Imager M1m motorized
194 microscope fitted with a PI piezo-motor scanning stage and an IDS μEye 4 Megapixel USB 3
195 CMOS digital camera. This was interfaced to a control PC using Trackworks software (Gleadow
196 et al., 2009; 2019). The true 3D lengths of the etched ²⁵²Cf semi-tracks were then measured
197 from the captured image stacks on a separate computer using FastTracks software (Gleadow
198 et al., 2009; 2019) until a maximum of 500 tracks per sample mount were attained, thus
199 totaling 1000 tracks per annealing experiment (500 on surfaces parallel to (100) and 500 on
200 the c-axis perpendicular surfaces). Track length measurements were made using both
201 reflected and transmitted light images and typically measured over ~30 grains. The surface
202 reflected light image was used to manually determine the center of the implanted ²⁵²Cf semi-
203 track etch pit, and the transmitted light stack for determining the position of the track
204 termination by scrolling down through the image stack to the last image plane where it
205 appeared clearly in focus. FastTracks automatically calculates true track lengths, correcting
206 the vertical focus depth for the refractive index of monazite, taken to be 1.794.

207
208 The equivalent confined track length (l) was then calculated based on a correction for the
209 small amount of surface lowering during track etching. This surface lowering during etching
210 on different planes was estimated from diameters of the track etch pits in different directions.
211 In uniaxial minerals, such as apatite and zircon, the dimensions of track etch pits are
212 satisfactorily described by the parameters Dpar and Dper (track diameters parallel and
213 perpendicular respectively to the c-axis, Donelick et al., 2005). However, for monoclinic
214 minerals, such as monazite, the situation is more complex, and we extend this terminology as
215 shown in Figure 1 with three track diameter measurements, Dpa (diameter parallel to the a-
216 axis), Dpb (parallel to b) and Dpc (parallel to c), the latter being equivalent to Dpar in apatite
217 and zircon. The track etch pits in monazite are rhombic in shape and in practice these three
218 diameter measurements are very similar to each other, so the differences are not critical
219 (Table 2).

Deleted: the

Deleted: c-axis parallel

Deleted: However

223

224 **Table 2.** Average diameters of implanted ²⁵²Cf fission track openings on both parallel and perpendicular surfaces
225 for each annealing schedule.

	Dpa (μm)	Dpb (μm)	Dpc (μm)
Surfaces // c-axis			
1 Hour	-	0.62	0.61
10 Hours	-	0.64	0.60
100 Hours	-	0.62	0.63
1000 Hours	-	0.61	0.60
Surfaces ⊥ c-axis			
1 Hour	0.62	0.61	-
10 Hours	0.62	0.63	-
100 Hours	0.63	0.64	-
1000 Hours	0.63	0.64	-
Average	0.63	0.62	0.61

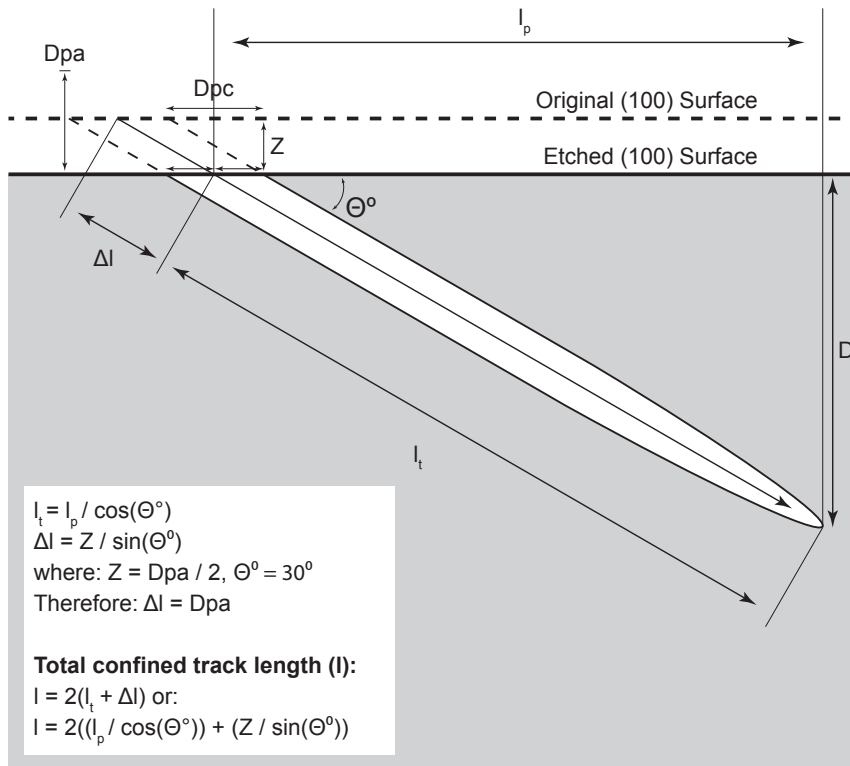
226

227

228 The track diameter measurements, representing the rate of etching from a point source in
229 different crystallographic orientations, may be used to estimate the rate of surface lowering
230 on different surfaces. For (100) surfaces (i.e. parallel to both b- and c-axes), the amount of
231 surface etching was estimated using measurements of the track width parameter Dpa,
232 measured on the surface normal to the c-axis (approximately parallel to the a- and b-axes).
233 Diameter measurements were made for approximately 250 tracks for both surface
234 orientations in each sample. The amount of surface etching on (100) was approximated by
235 half the mean Dpa measurement for each sample (Ure, 2010). Knowing the track implantation
236 angle (30°), allows for the length of the lost portion of the implanted semi-tracks to be
237 calculated and added to the total track length (Ure, 2010) as illustrated in Figure 3. The
238 equivalent confined fission track length is then obtained by doubling the corrected mean
239 semi-track length. For surfaces cut perpendicular to the c-axis (approximately (001)), the
240 relevant measurement for the surface lowering correction is the half the mean Dpc measured
241 on the (100) surfaces.

242

Deleted:Page Break.....
¶



245
 246 **Figure 3.** Illustration of the measurements and calculations required to correct semi-track lengths for surface
 247 etching on a (100) face (ie parallel to b and c). Bulk etching removes the original surface by approximately half
 248 the width of the etch pit diameter parallel to the a-axis (Dpa) measured on the $\sim(001)$ face (modified from Ure
 249 2010).

250

251 **3. Results**

252 Table 3 and Figure 4 present the track length measurements from the isochronal annealing
 253 experiments in Harcourt Granodiorite monazite. All length measurements are presented as
 254 mean lengths of equivalent confined fission tracks calculated according to the geometry in
 255 Figure 3 and duplicated on surfaces orientated parallel to (100) and perpendicular to the
 256 crystallographic c-axis. The annealing schedules are presented as 1, 10, 100 and 1000 hours
 257 between temperatures of 30°C → 400°C.

258

Deleted: -

260 Unannealed fission track lengths for all control samples range from 10.12 ± 0.06 – $11.23 \pm$
261 $0.08 \mu\text{m}$, averaging $10.60 \pm 0.19 \mu\text{m}$. These vary by considerably more than the analytical
262 uncertainty and possible reasons for this are considered below. Across all annealing
263 experiments, mean lengths become progressively shorter, down to a minimum measured
264 length of $4.88 \mu\text{m}$ (10 hours, 300°C , perpendicular c-axis). Note that for all the annealed
265 samples the average lengths of tracks etched on surfaces perpendicular to the
266 crystallographic c-axis are always shorter than those on surfaces parallel to (100). However,
267 the same is not true for all of the control measurements on unannealed samples.

268

269 Track length reduction normalized to the mean length for the unannealed control samples
270 ($10.60 \mu\text{m}$) are also presented in Table 3. Normalized lengths start at 1 (control sample),
271 reducing to ~ 0.5 before dropping abruptly to zero by the next heating step. The shortest mean
272 track lengths were seen in the 10-hour experiments, where l/l_0 decreased to values of 0.502
273 and 0.460 (300°C , parallel and perpendicular surfaces, respectively).

274

275 **Table 3.** Isochronal laboratory annealing data for ^{252}Cf tracks in the Harcourt Granodiorite monazite (1σ errors).

Deleted: e

Deleted: average length of tracks orientated on

Deleted: c

Annealing Time	Annealing Temp (°C)	Surface Orientation	²⁵² Cf Track Length (μm)*	Z (μm)	Calculated Track Length (μm)**	// ₀ (r)	No. of Tracks
Control	~20	// (100)	4.60 ± 0.84	0.31	10.42 ± 0.08	1	500
1 Hour	50	// (100)	4.29 ± 0.82	0.30	9.78 ± 0.07	0.923 ± 0.010	500
1 Hour	100	// (100)	4.05 ± 0.69	0.32	9.36 ± 0.06	0.883 ± 0.009	500
1 Hour	200	// (100)	3.34 ± 0.73	0.34	8.02 ± 0.07	0.757 ± 0.009	500
1 Hour	300	// (100)	2.90 ± 0.73	0.31	7.02 ± 0.06	0.662 ± 0.008	500
1 Hour	320	// (100)	2.60 ± 0.82	0.31	6.42 ± 0.07	0.606 ± 0.008	500
1 Hour	400	// (100)	0	0	0	0	0
Control	~20	⊥ c-axis	5.00 ± 0.88	0.31	11.23 ± 0.08	1	500
1 Hour	50	⊥ c-axis	4.27 ± 0.82	0.30	9.74 ± 0.07	0.919 ± 0.009	500
1 Hour	100	⊥ c-axis	4.01 ± 0.72	0.31	9.24 ± 0.06	0.872 ± 0.008	500
1 Hour	200	⊥ c-axis	3.25 ± 0.70	0.32	7.76 ± 0.06	0.732 ± 0.007	500
1 Hour	300	⊥ c-axis	2.60 ± 0.74	0.32	6.48 ± 0.06	0.611 ± 0.007	500
1 Hour	320	⊥ c-axis	2.44 ± 0.73	0.33	6.18 ± 0.07	0.583 ± 0.007	500
1 Hour	400	⊥ c-axis	0	0	0	0	0
Control	~20	// (100)	4.82 ± 0.57	0.32	10.90 ± 0.05	1	500
10 Hours	50	// (100)	4.20 ± 0.71	0.30	9.60 ± 0.06	0.906 ± 0.007	500
10 Hours	100	// (100)	3.82 ± 0.62	0.33	8.94 ± 0.06	0.843 ± 0.007	500
10 Hours	150	// (100)	3.43 ± 0.64	0.34	8.22 ± 0.06	0.775 ± 0.007	500
10 Hours	200	// (100)	3.17 ± 0.60	0.30	7.54 ± 0.06	0.711 ± 0.006	500
10 Hours	250	// (100)	2.77 ± 0.69	0.34	6.88 ± 0.06	0.649 ± 0.006	500
10 Hours	300	// (100)	2.03 ± 0.72	0.32	5.32 ± 0.06	0.502 ± 0.006	500
10 Hours	350	// (100)	0	0	0	0	0
Control	~20	⊥ c-axis	4.65 ± 0.53	0.33	10.62 ± 0.05	1	500
10 Hours	50	⊥ c-axis	4.15 ± 0.69	0.31	9.54 ± 0.06	0.900 ± 0.007	500
10 Hours	100	⊥ c-axis	3.81 ± 0.54	0.30	8.82 ± 0.05	0.832 ± 0.006	500
10 Hours	150	⊥ c-axis	3.40 ± 0.68	0.30	8.00 ± 0.06	0.755 ± 0.007	500
10 Hours	200	⊥ c-axis	3.09 ± 0.66	0.30	7.38 ± 0.06	0.696 ± 0.007	500
10 Hours	250	⊥ c-axis	2.63 ± 0.66	0.33	6.56 ± 0.06	0.619 ± 0.006	500
10 Hours	300	⊥ c-axis	1.81 ± 0.71	0.32	4.88 ± 0.06	0.460 ± 0.006	500
10 Hours	350	⊥ c-axis	0	0	0	0	0
Control	~20	// (100)	4.85 ± 0.75	0.30	10.90 ± 0.07	1	500
100 Hours	30	// (100)	4.46 ± 0.90	0.30	10.12 ± 0.08	0.955 ± 0.009	500
100 Hours	50	// (100)	4.19 ± 0.94	0.31	9.62 ± 0.08	0.908 ± 0.009	500
100 Hours	100	// (100)	3.75 ± 0.68	0.30	8.70 ± 0.06	0.821 ± 0.008	500
100 Hours	150	// (100)	3.32 ± 0.80	0.34	7.98 ± 0.07	0.753 ± 0.008	500
100 Hours	200	// (100)	3.04 ± 0.70	0.34	7.44 ± 0.06	0.702 ± 0.007	500
100 Hours	250	// (100)	2.51 ± 0.73	0.32	6.28 ± 0.07	0.592 ± 0.007	500
100 Hours	300	// (100)	0	0	0	0	0
100 Hours	350	// (100)	0	0	0	0	0
Control	~20	⊥ c-axis	4.50 ± 0.76	0.30	10.20 ± 0.07	1	500
100 Hours	30	⊥ c-axis	4.26 ± 0.84	0.32	9.80 ± 0.08	0.925 ± 0.010	500
100 Hours	50	⊥ c-axis	4.05 ± 0.83	0.33	9.42 ± 0.07	0.889 ± 0.009	500
100 Hours	100	⊥ c-axis	3.65 ± 0.63	0.31	8.54 ± 0.06	0.806 ± 0.008	500
100 Hours	150	⊥ c-axis	3.31 ± 0.74	0.32	7.90 ± 0.07	0.745 ± 0.008	500
100 Hours	200	⊥ c-axis	3.01 ± 0.69	0.32	7.28 ± 0.06	0.687 ± 0.008	499
100 Hours	250	⊥ c-axis	2.49 ± 0.53	0.32	6.24 ± 0.05	0.589 ± 0.006	500
100 Hours	300	⊥ c-axis	0	0	0	0	0
100 Hours	350	⊥ c-axis	0	0	0	0	0
Control	~20	// (100)	4.46 ± 0.64	0.30	10.12 ± 0.06	1	500
1000 Hours	50	// (100)	4.03 ± 0.60	0.30	9.26 ± 0.06	0.874 ± 0.008	500
1000 Hours	150	// (100)	3.18 ± 0.54	0.31	7.60 ± 0.05	0.717 ± 0.007	500
1000 Hours	200	// (100)	3.04 ± 0.74	0.30	7.28 ± 0.07	0.687 ± 0.007	500
1000 Hours	250	// (100)	2.60 ± 0.96	0.31	6.42 ± 0.09	0.606 ± 0.007	500
1000 Hours	275	// (100)	0	0	0	0	0
Control	~20	⊥ c-axis	4.58 ± 0.65	0.31	10.40 ± 0.06	1	500
1000 Hours	50	⊥ c-axis	3.99 ± 0.60	0.30	9.18 ± 0.06	0.866 ± 0.008	500
1000 Hours	150	⊥ c-axis	3.15 ± 0.52	0.31	7.56 ± 0.05	0.713 ± 0.006	500
1000 Hours	200	⊥ c-axis	2.79 ± 0.59	0.33	6.88 ± 0.05	0.649 ± 0.006	500
1000 Hours	250	⊥ c-axis	2.02 ± 1.08	0.33	5.36 ± 0.16	0.506 ± 0.008	187
1000 Hours	275	⊥ c-axis	0	0	0	0	0

* ± sd, ** ± se

Z is the amount of surface lowering due to bulk etching
//₀ (r) has been normalized to average control sample of 10.60 μm

Annealing Time	Annealing Temp (°C)	Surface Orientation	²⁵² Cf Track Length (μm)*	Z (μm)	Calculated Track Length (μm)**	// ₀ (r)	No. of Tracks
Control	~20	// c-axis	4.60 ± 0.84	0.31	10.42 ± 0.08	1	500
1 Hour	50	// c-axis	4.29 ± 0.82	0.30	9.78 ± 0.07	0.923 ± 0.010	500
1 Hour	100	// c-axis	4.05 ± 0.69	0.32	9.36 ± 0.06	0.883 ± 0.009	500
1 Hour	200	// c-axis	3.34 ± 0.73	0.34	8.02 ± 0.07	0.757 ± 0.009	500
1 Hour	300	// c-axis	2.90 ± 0.73	0.31	7.02 ± 0.06	0.662 ± 0.008	500
1 Hour	320	// c-axis	2.60 ± 0.82	0.31	6.42 ± 0.07	0.606 ± 0.008	500
1 Hour	400	// c-axis	0	0	0	0	0
Control	~20	⊥ c-axis	5.00 ± 0.88	0.31	11.23 ± 0.08	1	500
1 Hour	50	⊥ c-axis	4.27 ± 0.82	0.30	9.74 ± 0.07	0.919 ± 0.009	500
1 Hour	100	⊥ c-axis	4.01 ± 0.72	0.31	9.24 ± 0.06	0.872 ± 0.008	500
1 Hour	200	⊥ c-axis	3.25 ± 0.70	0.32	7.76 ± 0.06	0.732 ± 0.007	500
1 Hour	300	⊥ c-axis	2.60 ± 0.74	0.32	6.48 ± 0.06	0.611 ± 0.007	500
1 Hour	320	⊥ c-axis	2.44 ± 0.73	0.33	6.18 ± 0.07	0.583 ± 0.007	500
1 Hour	400	⊥ c-axis	0	0	0	0	0
Control	~20	// c-axis	4.82 ± 0.57	0.32	10.90 ± 0.05	1	500
10 Hours	50	// c-axis	4.20 ± 0.71	0.30	9.60 ± 0.06	0.906 ± 0.007	500
10 Hours	100	// c-axis	3.82 ± 0.62	0.33	8.94 ± 0.06	0.843 ± 0.007	500
10 Hours	150	// c-axis	3.43 ± 0.64	0.34	8.22 ± 0.06	0.775 ± 0.007	500
10 Hours	200	// c-axis	3.17 ± 0.60	0.30	7.54 ± 0.06	0.711 ± 0.006	500
10 Hours	250	// c-axis	2.77 ± 0.69	0.34	6.88 ± 0.06	0.649 ± 0.006	500
10 Hours	300	// c-axis	2.03 ± 0.72	0.32	5.32 ± 0.06	0.502 ± 0.006	500
10 Hours	350	// c-axis	0	0	0	0	0
Control	~20	⊥ c-axis	4.65 ± 0.53	0.33	10.62 ± 0.05	1	500
10 Hours	50	⊥ c-axis	4.15 ± 0.69	0.31	9.54 ± 0.06	0.900 ± 0.007	500
10 Hours	100	⊥ c-axis	3.81 ± 0.54	0.30	8.82 ± 0.05	0.832 ± 0.006	500
10 Hours	150	⊥ c-axis	3.40 ± 0.68	0.30	8.00 ± 0.06	0.755 ± 0.007	500
10 Hours	200	⊥ c-axis	3.09 ± 0.66	0.30	7.38 ± 0.06	0.696 ± 0.007	500
10 Hours	250	⊥ c-axis	2.63 ± 0.66	0.33	6.56 ± 0.06	0.619 ± 0.006	500
10 Hours	300	⊥ c-axis	1.81 ± 0.71	0.32	4.88 ± 0.06	0.460 ± 0.006	500
10 Hours	350	⊥ c-axis	0	0	0	0	0
Control	~20	// c-axis	4.85 ± 0.75	0.30	10.90 ± 0.07	1	500
100 Hours	30	// c-axis	4.46 ± 0.90	0.30	10.12 ± 0.08	0.955 ± 0.009	500
100 Hours	50	// c-axis	4.19 ± 0.94	0.31	9.62 ± 0.08	0.908 ± 0.009	500
100 Hours	100	// c-axis	3.75 ± 0.68	0.30	8.70 ± 0.06	0.821 ± 0.008	500
100 Hours	150	// c-axis	3.32 ± 0.80	0.34	7.98 ± 0.07	0.753 ± 0.008	500
100 Hours	200	// c-axis	3.04 ± 0.70	0.34	7.44 ± 0.06	0.702 ± 0.007	500
100 Hours	250	// c-axis	2.51 ± 0.73	0.32	6.28 ± 0.07	0.592 ± 0.007	500
100 Hours	300	// c-axis	0	0	0	0	0
100 Hours	350	// c-axis	0	0	0	0	0
Control	~20	⊥ c-axis	4.50 ± 0.76	0.30	10.20 ± 0.07	1	500
100 Hours	30	⊥ c-axis	4.26 ± 0.84	0.32	9.80 ± 0.08	0.925 ± 0.010	500
100 Hours	50	⊥ c-axis	4.05 ± 0.83	0.33	9.42 ± 0.07	0.889 ± 0.009	500
100 Hours	100	⊥ c-axis	3.65 ± 0.63	0.31	8.54 ± 0.06	0.806 ± 0.008	500
100 Hours	150	⊥ c-axis	3.31 ± 0.74	0.32	7.90 ± 0.07	0.745 ± 0.008	500
100 Hours	200	⊥ c-axis	3.01 ± 0.69	0.32	7.28 ± 0.06	0.687 ± 0.008	499
100 Hours	250	⊥ c-axis	2.49 ± 0.53	0.32	6.24 ± 0.05	0.589 ± 0.006	500
100 Hours	300	⊥ c-axis	0	0	0	0	0
100 Hours	350	⊥ c-axis	0	0	0	0	0
Control	~20	// c-axis	4.46 ± 0.64	0.30	10.12 ± 0.06	1	500
1000 Hours	50	// c-axis	4.03 ± 0.60	0.30	9.26 ± 0.06	0.874 ± 0.008	500
1000 Hours	150	// c-axis	3.18 ± 0.54	0.31	7.60 ± 0.05	0.717 ± 0.007	500
1000 Hours	200	// c-axis	3.04 ± 0.74	0.30	7.28 ± 0.07	0.687 ± 0.007	500
1000 Hours	250	// c-axis	2.60 ± 0.96	0.31	6.42 ± 0.09	0.606 ± 0.007	500
1000 Hours	275	// c-axis	0	0	0	0	0
Control	~20	⊥ c-axis	4.58 ± 0.65	0.31	10.40 ± 0.06	1	500
1000 Hours	50	⊥ c-axis	3.99 ± 0.60	0.30	9.18 ± 0.06	0.866 ± 0.008	500
1000 Hours	150	⊥ c-axis	3.15 ± 0.52	0.31	7.56 ± 0.05	0.713 ± 0.006	500
1000 Hours	200	⊥ c-axis	2.79 ± 0.59	0.33	6.88 ± 0.05	0.649 ± 0.006	500
1000 Hours	250	⊥ c-axis	2.02 ± 1.08	0.33	5.36 ± 0.16	0.506 ± 0.008	187
1000 Hours	275	⊥ c-axis	0	0	0	0	0

* ± sd, ** ± se

Z is the amount of surface lowering due to bulk etch
//₀ (r) has been normalized to average control sam

Deleted:

281

282 **4. Discussion**

283 The average track length for the unannealed control samples across all analyses is $10.60 \pm$
284 $0.19 \mu\text{m}$ which is slightly shorter but within error of the $11.30 \pm 0.36 \mu\text{m}$ mean length reported
285 by Ure (2010) for a smaller number of tracks in a different monazite of unknown composition.
286 Weise et al. (2009) calculated a mean range $8.30 \pm 0.62 \mu\text{m}$ for a heavy fission fragment and
287 $10.80 \pm 0.52 \mu\text{m}$ for a light fission fragment for ^{235}U fission in monazite. This combines to give
288 a total latent track length of $\sim 19 \mu\text{m}$. However, it has long been known (e.g. Fleischer et al.,
289 1975) that the lengths of etched fission tracks are significantly shorter than the total range of
290 the fission fragments due to a 'length deficit' of unetchable radiation damage towards the
291 end of the track. Weise et al. (2009) calculated the length deficit for an unannealed confined
292 fission track in monazite to be $6 - 7 \mu\text{m}$, making the etchable length for induced ^{235}U fission
293 tracks $\sim 12 - 13 \mu\text{m}$. Our measurements for the unannealed control samples are on average
294 $\sim 1 - 2 \mu\text{m}$ shorter than these estimates, suggesting that the length deficit may be closer to
295 $8 \mu\text{m}$ ($\sim 4 \mu\text{m}$ at each end) at least for the ^{252}Cf tracks used here. The mean track lengths
296 reported here are also broadly consistent with measured lengths of spontaneous ^{238}U
297 confined tracks, reported to be $\sim 10 \mu\text{m}$ (Weise et al., 2009).

298

299 There is a difference of $1.11 \mu\text{m}$ between the longest and shortest mean track lengths in
300 control samples across the experiments. This is substantial and significantly greater than the
301 measurement uncertainty. It is known that newly produced fission tracks in apatite undergo
302 rapid annealing at ambient temperatures (Donelick et al., 1990) from the moment the track
303 is formed in the crystal lattice until the track is etched. It was not clear whether this was due
304 to short-term thermal annealing or some non-thermal annealing mechanism. Belton (2006)
305 and Tamer and Ketcham (2020) also found similar effects in a series of ambient temperature
306 annealing experiments on freshly induced ^{235}U fission tracks in various apatites. The results
307 showed the tracks reduced in length by $0.32 - 0.70 \mu\text{m}$ between 39 seconds and 1.88 days
308 after irradiation and continued to shorten measurably over decades. While the exact amount
309 of time between ^{252}Cf track implantation and etching for each individual control sample was
310 not recorded in this study, the considerable length differences in the control samples suggest

Deleted: -

Deleted: -

Deleted: -

Deleted: -

315 that ambient temperature annealing may also occur in monazite, and probably to an even
316 greater degree than in apatite.

317

318 Differing degrees of ambient temperature annealing may also be the reason why mean track
319 lengths in monazite control samples cut perpendicular to the c-axis were not always shorter
320 than in those parallel to ~~the (100) face~~, as was invariably the case for all experiments at higher
321 temperatures. Further, Figure 4 shows that for all the isochronal experiments, the annealing
322 curves exhibit an initial length reduction of ~~~5–10%~~ before the 50°C annealing step, a feature
323 not observed in annealing experiments in other minerals. This may be due to the mean track
324 length for the control samples not having reached a stable value at ambient temperature
325 prior to the thermal annealing experiments.

326

327 Importantly, over the temperature range studied, no conditions have been identified where
328 the tracks are totally stable (Figure 4), even for experiments conducted at 30°C. Figure 4 also
329 shows that there is a gradual reduction in l/l_0 with temperature, followed by accelerated
330 reduction from ~ 0.580 to zero. For this reason, values of $l/l_0 < \sim 0.5$ are rarely encountered,
331 with only two slightly lower values (0.460 and 0.488) being observed amongst all 52
332 experiments. This is a similar behaviour to that seen in apatite and zircon (e.g. Green et al.,
333 1986; Yamada et al., 1995). Relatively less difference was observed between the averaged
334 track length reduction of the 100- and 1000- hour schedules compared to the shorter
335 annealing times.

336

Deleted: the c-axis

Deleted: -

Deleted: 2

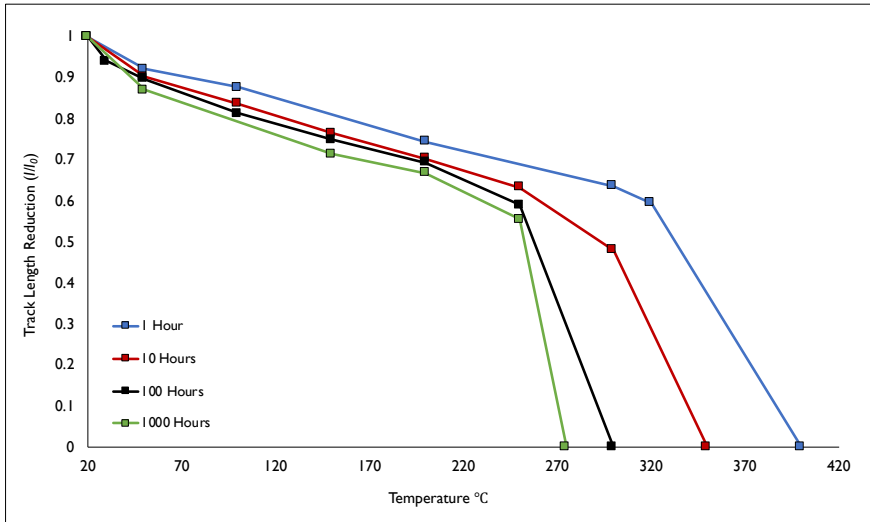
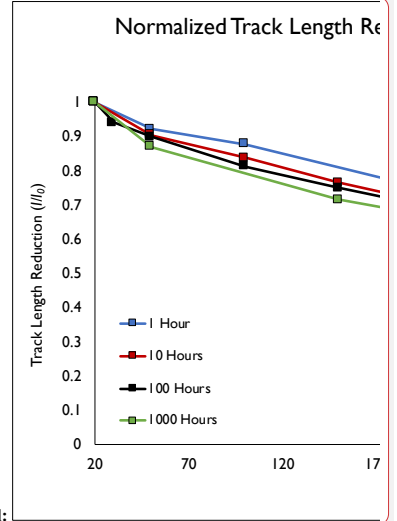


Figure 4. Normalized track length reduction (l/l_0) against temperature for calculated equivalent confined fission tracks in Harcourt Granodiorite monazite. The track length reduction values are averaged across both sets of surfaces ($//$ to (100) and \perp to the c-axis), with the normalized track length (l/l_0) values being calculated from the average length of the unannealed control samples (10.60 μm).

In all annealed samples, the mean equivalent confined track length was always less than that for the unannealed control samples. As annealing progresses, the mean track lengths are reduced and become consistently anisotropic with crystallographic orientation, although the differences are small and all within errors. Tracks implanted at 30° dip to polished surfaces oriented perpendicular to the crystallographic c-axis always have shorter mean track lengths than those at 30° to the (100) surfaces (as is the case for apatite, e.g. Green et al., 1986). On both these surface orientations the dips were constant but there was limited control on the azimuth orientations of the collimated tracks, so the exact relationship to crystallographic orientation is not clear. However, the distribution of track orientations will cover a different range on the two surfaces so that anisotropy of annealing can clearly be detected. As annealing progresses, the amount of anisotropy generally increases across all annealing schedules for the two surface orientations with the exception of 100 hours. That is, tracks on surfaces orientated perpendicular to the crystallographic c-axis anneal faster with increasing temperature. Anisotropy is still present in the 100-hour schedule, but no clear increase in the difference between calculated confined track lengths is apparent for the two differently



Deleted:

Deleted: T

Deleted: oth

Deleted:

Deleted: surfaces

Formatted: Font: 10 pt

Deleted: parallel ($//$) and perpendicular (

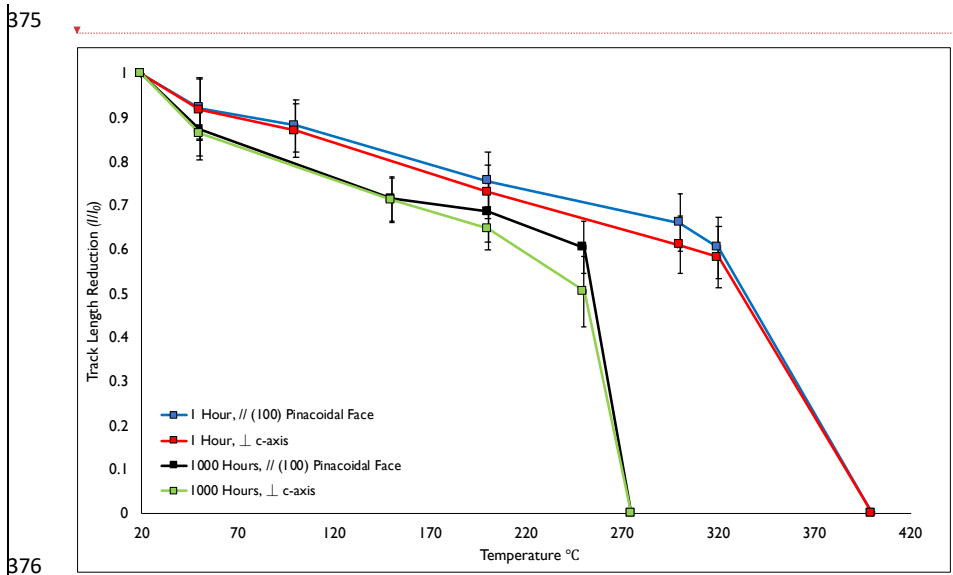
Deleted:)

Deleted: ,

Deleted: anisotropic with

Deleted: c-axis parallel

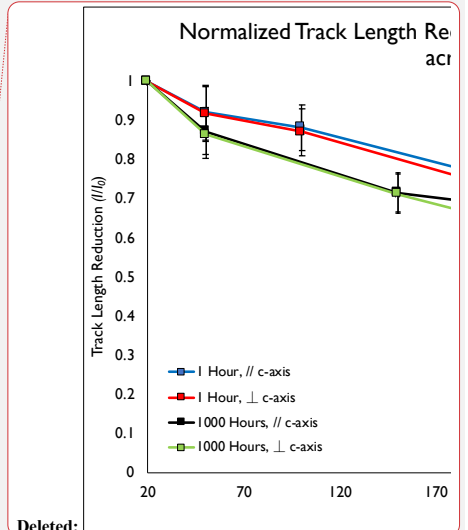
371 oriented surface planes. Anisotropy is greatest in the 1000 hours, 250°C experiments, where
 372 there is a ~1.06 μm difference between the two surface orientations (Figure 5). This is possibly
 373 due to only 187 semi-track lengths being measured in the c-axis perpendicular aliquot (as
 374 most were completely annealed) compared to 500 in the parallel aliquot.



376
 377 **Figure 5.** Normalized track length reduction (l/l_0) against temperature for calculated equivalent confined fission
 378 tracks for 1 and 1000 hour experiments for both surface orientations ($//$ and \perp surfaces, as in Figure 4). The
 379 normalized track length (l/l_0) values are calculated from the average length of the control samples (10.60 μm).
 380 Error bars refers to 1σ errors.

381
 382 Figure 6 shows the relationship between the standard deviation and mean track length for
 383 the length distributions of single fission fragment ^{252}Cf tracks. The results vary between 0.52
 384 and 1.08 μm and are mostly consistent with a mean of 0.71 μm but with considerable scatter.
 385 The results suggest an increase in standard deviation at short mean lengths, as is observed
 386 for confined track length measurements in apatite during annealing (e.g. Green et al., 1986,
 387 Fig 3) because of increasing anisotropy. For monazite, the amount of anisotropy also appears
 388 to increase as the mean track length decreases giving an increase in dispersion of individual
 389 track lengths, and hence standard deviation. The most extreme annealing observed is for the
 390 1000 Hours, 250°C experiment, with a standard deviation of 1.08 μm, which shows the

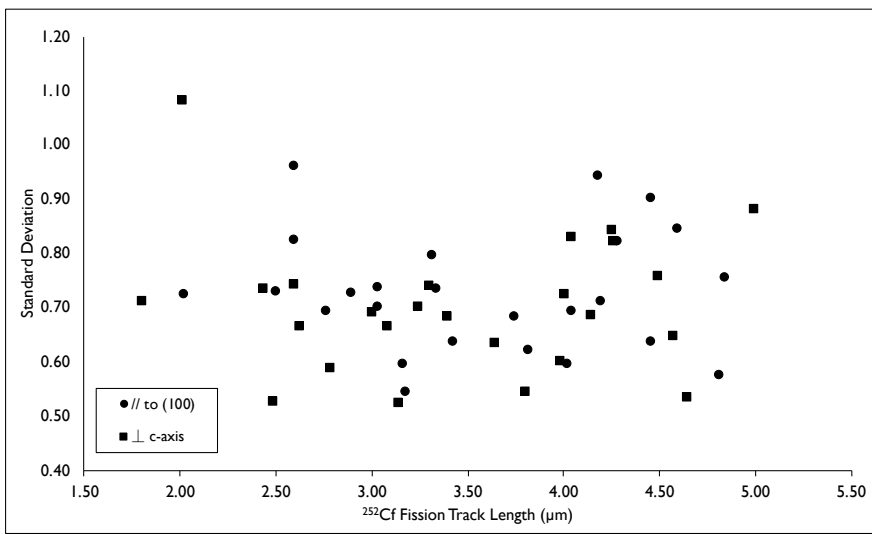
Deleted: ¶



Deleted:

Deleted: T

394 greatest degree of anisotropy. Although the results are highly scattered, it appears that there
 395 is a slight increase in standard deviation towards the longer mean track lengths. No
 396 explanation for such a trend is apparent, but we note that no similar effect has been observed
 397 in annealing experiments of confined track lengths in apatite (e.g., Green et al., 1986).

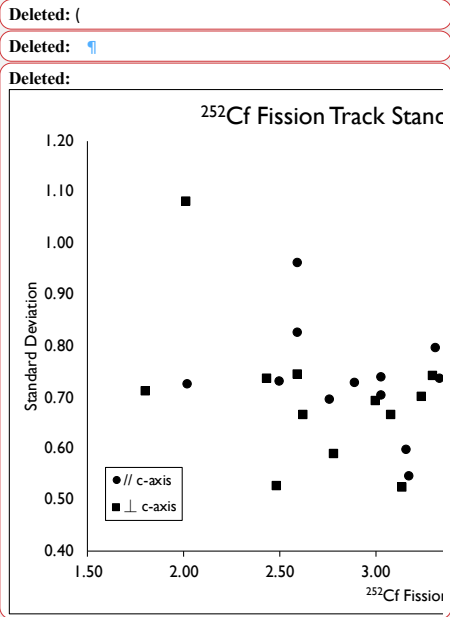


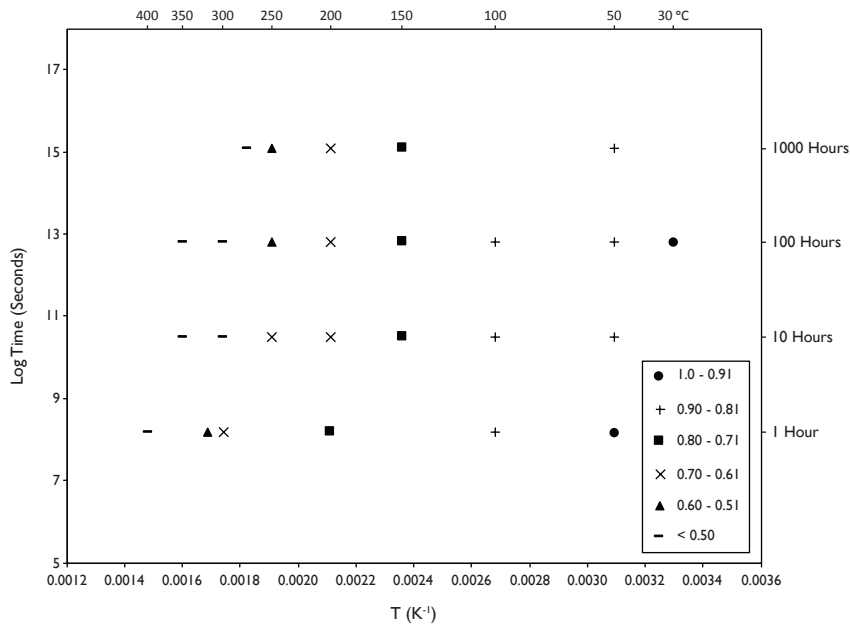
399
 400 **Figure 6.** Standard deviation of ²⁵²Cf fission-track length distributions plotted against their average track lengths
 401 for both parallel and perpendicular surfaces across all experiments.

402
 403 **5. The Arrhenius Plot**

404 Results of the Harcourt Granodiorite monazite annealing experiments are shown on an
 405 Arrhenius plot of log time versus inverse absolute temperature in Figure 7. Results are
 406 averaged across both surface orientations, and the normalized track length ($r=l/l_0$) values are
 407 calculated relative to the average length of the unannealed control samples ($l_0 = 10.60 \mu\text{m}$).
 408 In the plot, normalized track length values in a particular range are represented by the same
 409 symbol and exhibit linear trends with positive correlation. To extrapolate laboratory
 410 annealing results in Arrhenius plots to geological timescales, three types of model fitting have
 411 traditionally been used to determine a functional form of the fission track annealing kinetics,
 412 i.e. the 'parallel model' and two variations of the 'fanning model' (Laslett et al., 1987).

413





418
 419 **Figure 7.** Arrhenius plot of experimental data using calculated equivalent confined fission track lengths in
 420 Harcourt Granodiorite monazite. Each point represents two annealing experiments that have been averaged
 421 across both orientations (∥ and ⊥ surfaces, as in Figure 4). Different degrees of track length reduction (r) are
 422 shown by different symbols. Inverse absolute temperature in Kelvins, shown on the x-axis and corresponding
 423 temperatures in °C along the top.

Deleted: (parallel
 Deleted: and perpendicular to c-axis).
 Deleted: s

424
 425 **5.1 Parallel Linear Model**

426 As a starting point, the annealing data of this study will be tested with the 'parallel model'
 427 that has straight line contours (Laslett et al., 1987):

428
 429
$$\ln(t) = A(r) + B/T \quad (1)$$

430
 431 Where t = annealing time; T = annealing temperature (K); $A(r)$ = intercept of the lines (at $1/T$
 432 = 0), which is a function of the most reliable values of normalized mean length r ; and B is the
 433 slope, which is a constant for all degrees of annealing. The intercept $A(r)$ is subject to the
 434 following constraints: (1) $A(r)$ decreases monotonically with increasing r ; and (2) $A(r = 1) \rightarrow$

438 $-\infty$ when $t \rightarrow 0$, $T \rightarrow 0$. It should be noted that $r = 0$ for finite values of t and T provided they
439 are large enough, in practice.

440 The fully parameterized parallel model has the form:

441

$$\begin{aligned} 442 \quad r &= c_1 + c_2 A(r) + \varepsilon \\ 443 \quad &= c_1 + c_2 [\ln(t) - B/T] + \varepsilon \end{aligned} \quad (2)$$

444 or

$$445 \quad g(r; a, b) = C_0 + C_1 \ln(t) + C_2/T + \varepsilon \quad (3)$$

446

447 Where $C_0 = c_1$; $C_1 = c_2$; $C_2 = -c_2 B$; $g(r; a, b)$ is a transform containing r and two parameters a
448 and b ; and ε represents errors or residuals. ε is assumed to be normally distributed with mean
449 $\mu = 0$ and constant variance σ^2 . This assumption can be checked by residual plot for the model
450 in Figure 9. A single Box-Cox transformation was adopted and was found to be better suited
451 to the data than the double Box-Cox (Box and Cox, 1964):

452

$$453 \quad g(r; a, b) = [\{ (1 - r^b) / b \}^a - 1] / a \quad (4)$$

454

455 In the model of Eq. 3, parameters and uncertainties (standard error) were evaluated for the
456 data sets in Table 4 as follows:

457

$$\begin{aligned} 458 \quad a &= 1, & b &= 3.72 \\ 459 \quad C_0 &= -0.440275 \pm 0.034626, & C_1 &= -0.019504 \pm 0.002284 \end{aligned}$$

460

461 and

462

$$463 \quad C_2 = 437.315478 \pm 10.901345$$

464

465 **5.2 Fanning Linear Model**

466 The fanning Arrhenius plot of Laslett et al. (1987) has slopes of contour lines that change with
467 a variation of activation energy E with the degree of annealing. In this case, Eq. 1 becomes:

468

469 $\ln(t) = A(r) + B(r) / T$ (5)

470

471 where both slope $B(r)$ and intercept $A(r)$ are a function of r . A first order assumption of this
472 equation is that $A(r)$ is a negative linear function of $B(r)$:

473

474 $A(r) = c_3 - c_4 B(r)$ (6)

475

476 where c_3 and c_4 are constants, by analogy with the 'compensation law' for diffusion (e.g., Hart,
477 1981). This causes the contours to fade and meet at a single point on the Arrhenius plot.

478 Combining Eqs. 4 and 5 becomes:

479

480 $\ln(t) = A^* + B(r) [(1/T) - (1/T_0)]$ (7)

481

482 where $A^* = c_3$; and $1/T_0 = c_4$. T_0 is known as the "critical temperature", which is the
483 temperature of the 'cross-over point' of the fading contours (e.g. Crowley et al., 1991). Solving
484 Eq. 6 for $B(r)$ gives:

485

486 $B(r) = (\ln(t) - A^*) / [(1/T) - (1/T_0)]$ (8)

487

488 Constraints for slope $B(r)$ are: (1) $B(r)$ decreases monotonically with increasing r ; and (2) $B(r =$
489 $1) \rightarrow 0$ when $\ln(t) \rightarrow A^*$, $T \rightarrow 0$. The fully parameterized model is given as:

490

491 $r = c_1 + c_2 B(r) = c_1 + c_2 \{[\ln(t) - A^*] / [(1/T) - (1/T_0)]\} + \varepsilon$ (9)

492

493 or

494

495 $r = C_0 + (C_1 \ln(t) + C_2) / [(1/T) - C_3] + \varepsilon$ (10)

496

497 where $C_0 = c_1$; $C_1 = c_2$; $C_2 = -c_2 A^*$; and $C_3 = 1/T_0$.

498

499 When $C_3 = 0$, this assumes an infinite critical temperature (i.e., $T_0 = \infty$). The equation can be
500 rearranged to:

501

$$502 \quad r = C_0 + C_1 T \ln t + C_2 T + \varepsilon \quad (11)$$

503

504 The number of parameters is reduced from four to three, simplifying the equation. The
505 parameters and uncertainties (standard error) for the models in Eq. 10 were calculated as
506 follows:

$$507 \quad C_0 = 1.374 \pm 0.02698, \quad C_1 = -0.001105 \pm 0.00007301$$

508

509 and

510

$$511 \quad C_2 = -0.00002979 \pm 0.000004959$$

512

513 In the case where $T_0 \neq \infty$, Eq. 9 was adopted for the fitting calculation. The parameters and
514 uncertainties were evaluated as follows:

515

$$516 \quad C_0 = 1.227 \pm 0.09638, \quad C_1 = -0.00002418 \pm 0.000005221,$$

517

$$518 \quad C_2 = -0.0005491 \pm 0.0003005$$

519

520 and

521

$$522 \quad C_3 = -0.0005542 \pm 0.0003468$$

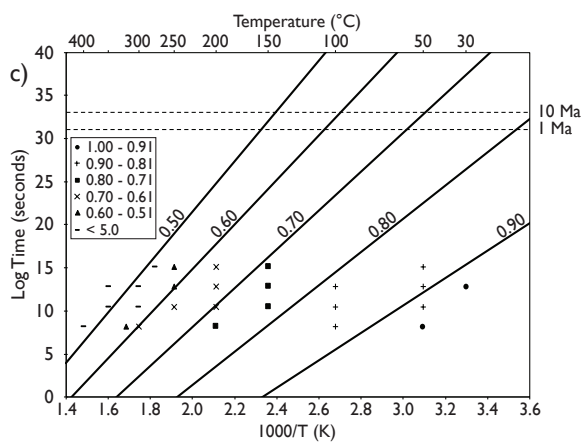
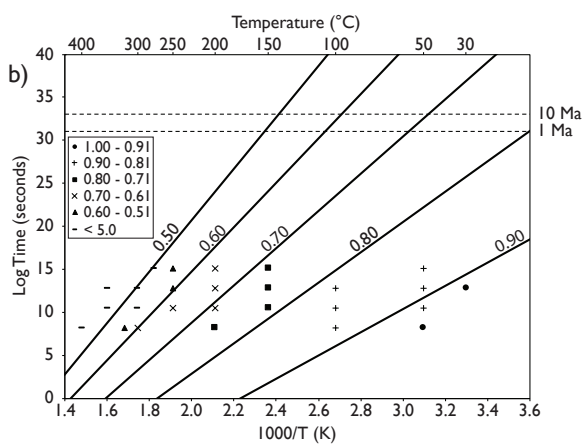
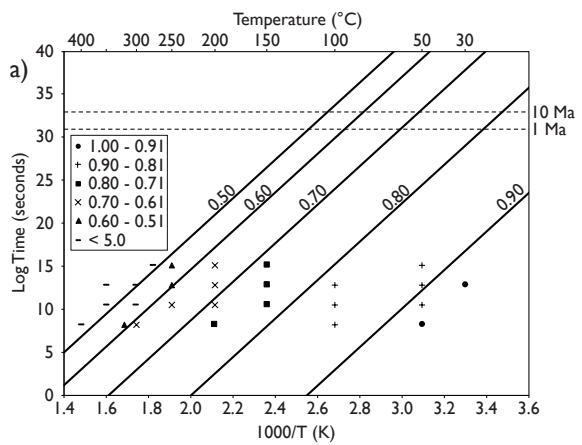
523

524 Both single and double Box-Cox transforms were applied to Eqs. 10 and 11. A single Box-Cox
525 transformation was better suited to fit the data; however, it did not statistically improve the
526 models. A t-test found that Eq. 11 with a single Box-Cox transformation had a P -value of 0.096.

527 Generally, a P -value < 0.05 suggests strong evidence against the null hypothesis and that it
528 should be rejected. Whereas a p -value > 0.05 indicates weak evidence against the null
529 hypothesis, failing to reject it. In the case of Eq. 11 the null hypothesis is the equation without

Deleted: -

531 a transformation and the alternative is to include the single Box-Cox transformation. Using a
532 similar form of test for Eq. 10 found that the C_3 constant produced a p -value of 0.123. This
533 high P -value suggests that the constant is not preferred and that the model from Eq. 11 is
534 more parsimonious. For these reasons, the final fanning models are presented with no
535 transformation (Eq. 10 and 11) and their assumptions can be checked in Figure 9.



537 **Figure 8.** Arrhenius plots with fitted lines extrapolated to geological timescales. (a) parallel model; (b) fanning
 538 model ($T_0 \neq \infty$); and (c) fanning model ($T_0 = \infty$). Each plot was obtained by adopting specific equations: (a) Eq. 3;
 539 (b) Eq. 10; and (c) Eq.11 (see text), and parameters as in Table 4. Values of normalized mean length (r) for each
 540 contour are indicated on the plots, ranging from 0.90 to 0.50. Symbols are the same as for Figure 5.

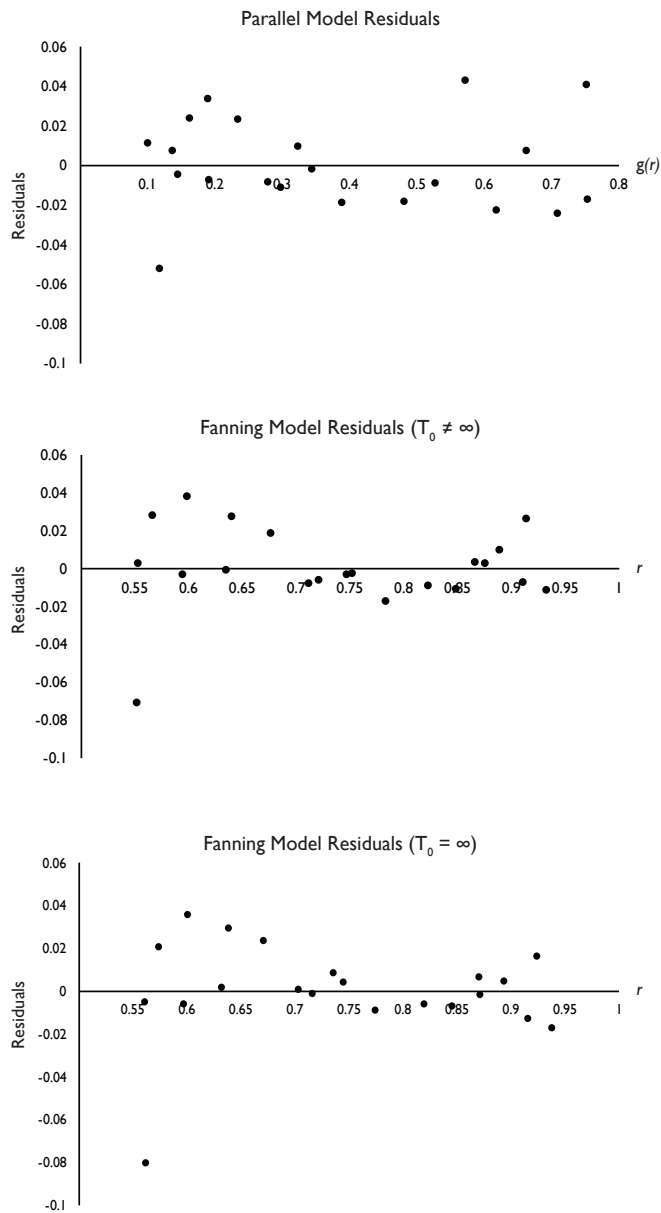
541

542 **Table 4.** Results of the Arrhenius model fitting calculations including estimated temperatures ($^{\circ}\text{C} \pm 2\sigma$ error) for
 543 the monazite partial annealing zone (MPAZ). Note the $T_0 \neq \infty$ estimated MPAZ has no error listed as it is not
 544 possible to reliably calculate the confidence intervals.

	Parallel Model	Fanning Model	
		$T_0 \neq \infty$	$T_0 = \infty$
Model Equation	Eq.3	Eq. 10	Eq. 11
Coefficient of Determination (R^2)	0.99	0.97	0.97
Bottom of MPAZ (2σ) ($^{\circ}\text{C}$)			
Heating Duration:			
1 Ma	-39.64 \pm 6.14	-82.52	-64.30 \pm 13.30
10 Ma	-44.11 \pm 6.49	-89.54	-71.12 \pm 13.78
Top of MPAZ (2σ) ($^{\circ}\text{C}$)			
Heating Duration:			
1 Ma	116.47 \pm 16.06	153.75	157.33 \pm 20.55
10 Ma	101.48 \pm 16.60	140.25	143.26 \pm 21.70

545

546



547
 548 **Figure 9.** Residual Plots for the best fitting calculations for each model (ε in Eqs. 3, 10 and 11). Each point
 549 represents one annealing experiment.

550

551 **5.3 Comparison of Arrhenius Models**

552 Table 4 and Figure 8 present the results of the model fitting calculations and their associated
553 Arrhenius plots. The models show the full data set with contours of equal length reduction
554 extrapolated to geological timescales. The parallel model, which has a constant activation
555 energy with decreasing r , statistically describes the data **marginally** better than the two
556 fanning models (coefficient of determination of 0.99 compared to 0.97 for both fanning
557 models). Nevertheless, the two fanning models, which have an increasing activation energy
558 with decreasing r , still describe the data very well. Although the coefficient of determination
559 of the two fanning models are equal, the P -value of 0.128 for constant C_3 in Eq. 10 suggests
560 that the simpler model is the more favourable. Residual plots for each model (Figure 9) show
561 no clear structure suggesting that the residuals do not contradict the linear assumption of the
562 models. In previous studies (e.g. Crowley et al., 1991; Laslett et al., 1987; Yamada et al., 1995),
563 both fanning models have a Box and Cox (1964) or similar type of transformation on the left-
564 hand side of the equation, but because they did not statistically improve them, they were
565 abandoned in this study. The fanning models, as they stand, explain the data very well, and
566 in general, when constructing empirical models to be used as the basis of prediction, simple
567 models with less fitted parameters are generally preferable (Laslett et al., 1987). Regardless
568 of using a transformation or not, all models presented in this study give a statistically
569 satisfactory description of the available data.

570

571 When comparing the models over laboratory timescales, little difference is observed between
572 them, particularly at length reductions < 0.80 . The 0.90 track reduction contour shows the
573 largest difference over laboratory timescales, where both fanning models splay out to lower
574 temperatures. This suggests that fission tracks in monazite are even more sensitive to low
575 temperature annealing in the fanning models compared to the parallel model. As with all such
576 annealing studies, differences in annealing are magnified when the data are extrapolated to
577 geological timescales. The assumption underlying such extrapolations is that track annealing
578 results from the same physical mechanism under both laboratory and geological conditions.
579 All models show that significant reduction in the etchable lengths of fission tracks takes place
580 at ambient and lower temperatures ($< 20^\circ\text{C}$) over geological timescales and that monazite is
581 particularly sensitive to low temperature thermal annealing. Considerably more track

Deleted: slightly

Deleted: 7

584 shortening would occur in the shallow upper crust between temperatures of ~50–160°C over
585 geological timescales of 1 – 10 Ma. Complete annealing of fission tracks occurred very rapidly
586 when the equivalent confined track length reduction decreased below ~0.5.

Deleted: -

587
588 Weise et al. (2009) presented a linear fanning model that used contours representing the
589 amount of track length reduction of implanted Kr-tracks in monazite rather than the
590 normalised reduction (l/l_0) as used here. However, similarities can be seen between the
591 different approaches. Both models show considerable track annealing at ambient surface
592 temperatures or below over geological timescales. That is, they are in agreement that a total
593 fission track stability zone is absent for monazite.

594
595 As highlighted in Laslett et al. (1987), there is no good reason why the contours in the fanning
596 Arrhenius plot need to be straight and an alternative fanning curvilinear model has been
597 proposed in the case of apatite by Ketcham et al. (2007, 1999). It is not possible to evaluate
598 such a fanning curvilinear model for monazite from the available data and many more data
599 points, especially for even longer heating schedules, would be required.

601 6. Estimation of the monazite partial annealing zone

602 Geological temperature ranges for the monazite partial annealing zone (MPAZ) were
603 calculated by extrapolating model equations to the geological timescale with parameters
604 derived from the annealing experiments (Table 4). The temperature limits of the MPAZ are
605 here approximated to be $l/l_0 = 0.95$ and 0.50 because measurements are difficult and
606 imprecise outside this range (c.f. Green et al., 1986 for apatite and Yamada et al., 1995 for
607 zircon). Track length reductions below this threshold are rarely observed (see Figure 4). The
608 parallel model (Figure 8a) shows estimates of the MPAZ for a heating duration of 10^7 years ~-
609 44 – 101°C. Both fanning models estimate a wider temperature range for the same heating
610 duration: -89 – 140°C ($T_0 \neq \infty$); and -71 – 143°C ($T_0 = \infty$). The uncertainties of estimated
611 temperatures are ca. ± 6 – 21°C for Eqs. 3 and 11 (2 standard errors). The bootstrapping
612 method for calculating the uncertainties of the estimated MPAZ temperatures could not be
613 confidently calculated for Eq. 10 and therefore error estimates have not been included for
614 this model. The inability to confidently calculate the uncertainties of Eq. 10 further supports

Deleted: lower

Deleted: has been

Deleted: defined

Deleted: as

Deleted: (

Deleted: ,

Deleted:)

Deleted: (

Deleted:)

Deleted: , since a track length reduction at the 5% level should be clearly detectable under the microscope

Deleted: The higher temperature limit of the MPAZ is defined at $l/l_0 = 0.50$, which corresponds with the final rapid fading of tracks observed in this study.

Deleted: -

Deleted: -

632 the choice of Eq. 11 ($T_0 = \infty$) as the preferred fanning model. Of the two remaining estimates
633 for the MPAZ range (Eqs. 3 and 11), based on the coefficients of determination, the parallel
634 model is slightly preferable. However, the fanning model of Eq. 11 also describes the data
635 almost as well and should not be ruled out. In fact, annealing studies of other minerals such
636 as zircon and apatite have shown a fanning model to best fit their respective datasets (e.g.
637 Ketcham et al., 1999; Laslett et al., 1987; Yamada et al., 1995).

638
639 Taking the fission track closure temperature (T_c) to be approximately the middle of the MPAZ,
640 predicted closure temperatures for the monazite fission track system range between $\sim 45 -$
641 25°C over geological timescales of $10^6 - 10^7$ years. These results are consistent with the
642 findings of Weise et al. (2009), the only other study to estimate a T_c for the monazite fission
643 track system, who estimated T_c to be $< 50^\circ\text{C}$ and perhaps not much above ambient.

644 **7. Conclusions**

645
646 Using implanted ^{252}Cf semi-tracks, isochronal annealing experiments were performed on
647 monazite crystals from the Harcourt Granodiorite in Central Victoria. Semi-track lengths were
648 measured and combined with an estimate of the degree of surface etching to give calculated
649 equivalent confined fission track lengths. The unannealed equivalent confined fission track
650 lengths (control samples) have a mean length of $10.60 \pm 0.19 \mu\text{m}$, which is broadly consistent
651 with the measured lengths of spontaneous ^{238}U confined tracks reported by Weise et al.
652 (2009). As annealing progresses, the mean calculated confined track length decreases
653 anisotropically to a small degree. Tracks on surfaces parallel to (100) and perpendicular to the
654 c-axis anneal at slightly different rates, but the differences are much smaller than observed
655 in apatite.

656
657 Using the equations of Laslett et al. (1987), three empirical models describe the data very
658 well, with the parallel Arrhenius plot fitting the data slightly better than two alternative
659 fanning models. The differences between these models are negligible, however, and for
660 consistency with annealing behaviour in other minerals (e.g., Green et al., 1986; Yamada et
661 al., 1995) the simpler fanning model (Eq. 11, $T_0 = \infty$) is preferred. Extrapolation of the data to
662 geological timescales suggest that fission tracks in monazite are very sensitive to low

Formatted: Not Superscript/ Subscript

Deleted: closure temperature (T_c)

Deleted: (Yamada et al., 1995)

Deleted: -

Deleted: The

Deleted: ¶

Deleted: ,

Deleted: with t

Deleted: and parallel

Deleted: the crystallographic

Deleted:

Deleted: ing

Deleted: measurably

Deleted: .

Deleted: ¶

Deleted: remarkably

Deleted: , and, in line with experience in other minerals

Deleted: a fanning model

Deleted: is preferred

Deleted: (

682 temperature annealing and that significant shortening of tracks occurs even at ambient
683 surface temperatures (~20°C) and below. Continued shortening of tracks occurs at
684 temperatures between ~50 – 160°C when extrapolated to geological timescales, with few
685 tracks being recorded at lengths of $l/l_0 < 0.5$. Closure temperatures for fission track retention
686 in monazite are estimated to be only 46 – 25°C over geological timescales of $10^6 - 10^7$ years,
687 consistent with the <50°C estimate of Weise et al. (2009).

688
689 There are a range of factors that have not been considered in this study that could possibly
690 influence annealing kinetics. These include compositional variations, a known factor
691 influencing the rate of fission track annealing in apatite (e.g. Green et al., 1985), which can
692 only be evaluated by further work on a much wider range of monazite compositions. A second
693 factor is the possibility of radiation enhanced annealing (e.g. McDannell et al. 2019). The
694 extremely high actinide content might suggest that monazite should show any such effect to
695 a greater degree than other minerals studied to date. Establishing the purely thermal
696 annealing properties (this study and Weise et al., 2009) is an essential first step for evaluating
697 any such effect in monazite. Our results suggest that thermal annealing alone may be
698 sufficient to explain the relatively young fission track ages previously reported in monazite.

699
700 Further confirmation of our preferred annealing model will require detailed comparison of
701 our observations with natural field examples and borehole studies. Nevertheless, it is clear
702 that fission tracks in monazite have the lowest thermal stability of any mineral so far studied
703 and this system has potential for use as an ultra-low temperature thermochronometer.

704

705 **Author Contributions**

706 SJ is a PhD student who obtained and analysed the presented data as well as prepared the
707 original manuscript. AG and BK provided supervision and contributed to several drafts of the
708 original manuscript. Sample material was provided by AG and BK.

709

710 **Competing Interests**

711 The authors declare that they have no conflict of interest.

712

713 **Acknowledgements**

Deleted: -

Deleted: -

Deleted: ¶

Deleted: ¶

As highlighted in Laslett et al. (1987), there is no good reason why the contours in the fanning Arrhenius plot need to be straight and an alternative fanning curvilinear model has been proposed in the case of apatite by Ketcham et al. (2007, 1999). Further experiments to increase the number of data points, especially for even longer heating schedules, would be required to test this model in monazite. Factors that have not been considered in this study and could possibly influence annealing kinetics are compositional effects (e.g. Green et al., 1985), radiation damage effects on etching (e.g. Gleadow, 1981) and radiation enhanced annealing (e.g. McDannell et al. 2019). The validity of this study still requires further confirmation by comparing the predictions from our laboratory results with observations from natural field examples and borehole studies. Nevertheless, it is clear that fission tracks in monazite have the lowest thermal stability of any mineral so far studied and this system has potential for use as an ultra-low temperature thermochronometer. ¶

Field Code Changed

Deleted: (

Deleted: ,

739 We thank Ling Chung for assistance and advice on sample preparation methods and Cameron
740 Patrick from The University of Melbourne Statistical Consulting Centre for assistance with
741 statistical analysis. [SJ also acknowledges funding from the Australian Government through
742 the Research Training Program \(RTP\) Scholarship.](#) The Melbourne thermochronology
743 laboratory is supported by the AuScope Program funded under the National Collaborative
744 Research Infrastructure Strategy (NCRIS). [We thank Ewald Hejl and Dale Issler for their
745 constructive reviews that have substantially improved the manuscript and Cornelia Spiegel
746 for editorial oversight.](#)

Deleted: SJ also acknowledges funding from the Australian Government through an Australian Postgraduate Award (APA). ...

747

748 **References**

Deleted: ¶

749 [Badr, M. J., Masoudi, F., Collins, A. S., and Cox, G.: Dating of Precambrian Metasedimentary
750 Rocks and Timing of their Metamorphism in the Soursat Metamorphic Complex \(NW
751 IRAN\): Using LA–CP–MS , U – Pb Dating of Zircon and Monazite, Journal of Sciences,
752 21\(4\), 311–319, 2010.](#)

753 [Belton, D. X.: The low-temperature thermochronology of cratonic terranes, Ph.D. thesis,
754 School of Earth Sciences, The University of Melbourne, 2006.](#)

755 [Box, G. E. P., and Cox, D. R.: An Analysis of Transformations, J Roy Stat Soc B Met., 26\(2\),
756 211–252, 1964.](#)

757 [Cenki-Tok, B., Berger, A., and Gueydan, F.: Formation and preservation of biotite - rich
758 microdomains in high - temperature rocks from the Antananarivo Block, Madagascar,
759 Int J Earth Sci., 105\(5\), 1471–1483, <https://doi.org/10.1007/s00531-015-1265-0>, 2016.](#)

760 [Clemens, J. D.: Granitic magmas with I-type affinities, from mainly metasedimentary
761 sources: the Harcourt batholith of southeastern Australia, Contrib Mineral Petr,
762 173\(11\), 1–20, <https://doi.org/10.1007/s00410-018-1520-z>, 2018.](#)

763 [Crowley, K. d., Cameron, M., and Schaefer, R. I.: Experimental studies of annealing of etched
764 fission tracks in fluorapatite, Geochim Cosmochim Ac., 55\(5\), 1449–1465,
765 \[https://doi.org/10.1016/0016-7037\\(91\\)90320-5\]\(https://doi.org/10.1016/0016-7037\(91\)90320-5\), 1991.](#)

766 [Donelick, Raymond A., Roden, M. K., Mooers, J. D., Carpenter, B. S., and Miller, D. S.:
767 Etchable length reduction of induced fission tracks in apatite at room temperature \(~
768 23°C\): Crystallographic orientation effects and “initial” mean lengths, International
769 Journal of Radiation Applications and Instrumentation. Part, 17\(3\), 261–265.
770 \[https://doi.org/10.1016/1359-0189\\(90\\)90044-X\]\(https://doi.org/10.1016/1359-0189\(90\)90044-X\), 1990.](#)

775 [Donelick, R. A., O'Sullivan, P. B., and Ketcham, R. A.: Apatite Fission-Track Analysis. Rev](#)
776 [Mineral Geochem., 58\(1\), 49–94, <https://doi.org/10.2138/rmg.2005.58.3>, 2005.](#)
777 [Fayon, A. K.: Fission Track Dating of Monazite: Etching Efficiencies as a Function of U](#)
778 [Content, in: GSA Annual Meeting, Geological Society of America, Minneapolis, p. 331,](#)
779 [2011.](#)
780 [Fleischer, R. L., Price, P. B., and Walker, R. M.: Nuclear Tracks in Solids, Berkeley: University](#)
781 [of California Press, 1975.](#)
782 [Gleadow, A. J. W.: Fission-track dating methods: What are the real alternatives? Nuclear](#)
783 [Tracks, 5, 3–14, \[https://doi.org/10.1016/0191-278X\\(81\\)90021-4\]\(https://doi.org/10.1016/0191-278X\(81\)90021-4\), 1981.](#)
784 [Gleadow, A. J. W., Raza, A., Kohn, B. P., and Spencer, S. A. S.: The potential of monazite as a](#)
785 [new low-temperature fission-track thermochronometer, 10th International Conference](#)
786 [on Fission Track Dating, Amsterdam, 2004.](#)
787 [Gleadow, A. J. W., Gleadow, S. J., Frei, S., Kohlmann, F., and Kohn, B. P.: Automated](#)
788 [analytical techniques for fission track thermochronology, Geochim Cosmochim Ac.](#)
789 [Supplement, 73, A441, 2009.](#)
790 [Gleadow, A., Kohn, B., & Seiler, C.: The Future of Fission-Track Thermochronology, in:](#)
791 [Fission-Track Thermochronology and its Application to Geology, edited by: Malusà, M.](#)
792 [and Fitzgerald, P., Springer, 77–92, 2019.](#)
793 [Green, P. F., Duddy, I. R., Gleadow, A. J. W., Tingate, P. R., and Laslett, G. M.: Fission-track](#)
794 [annealing in apatite: Track length measurements and the form of the Arrhenius plot,](#)
795 [Nucl Tracks Rad Meas., 10\(3\), 323–328, \[https://doi.org/10.1016/0735-245X\\(85\\)90121-\]\(https://doi.org/10.1016/0735-245X\(85\)90121-8\)](#)
796 [8, 1985.](#)
797 [Green, P. F., Duddy, I. R., Gleadow, A. J. W., Tingate, P. R., and Laslett, G. M.: Thermal](#)
798 [annealing of fission tracks in apatite 1. Variable temperature behaviour, Chem Geol.:](#)
799 [Isotope Geoscience Section, 59, 237–253, \[https://doi.org/10.1016/0168-\]\(https://doi.org/10.1016/0168-9622\(88\)90019-X\)](#)
800 [9622\(88\)90019-X, 1986.](#)
801 [Hart, S. R.: Diffusion compensation in natural silicates, Geochim Cosmochim Ac., 45, 279–](#)
802 [291, 1981.](#)
803 [Jones, S., Gleadow, A., Kohn, B., and Reddy, S. M.: Etching of fission tracks in monazite: An](#)
804 [experimental study, Terra Nova \(Special Issue-Thermo2018\), 1–10,](#)
805 [https://doi.org/10.1111/ter.12382, 2019.](#)
806 [Ketcham, R. A., Donelick, R. A., and Carlson, W. D.: Variability of apatite fission-track](#)

annealing kinetics: III. Extrapolation to geological time scales, *Am Mineral.*, 84, 1213–1223, 1999.

Ketcham, R. A., Carter, A., Donelick, R. A., Barbarand, J. B., and Hurford, A. J.: Improved modeling of fission-track annealing in apatite, *Am Mineral.*, 92(1), 799–810, <https://doi.org/10.2138/am.2007.2281>, 2007.

Laslett, G. M., Green, P. F., Duddy, I. R., and Gleadow, A. J. W.: Thermal annealing of fission tracks in apatite 2. A quantitative analysis, *Chem Geol.: Isotope Geoscience Section*, 65(1), 1–13, [https://doi.org/10.1016/0168-9622\(87\)90057-1](https://doi.org/10.1016/0168-9622(87)90057-1), 1987.

Malusa, M. G., and Fitzgerald, P. G. (Eds.): *Fission-Track Thermochronology and its Application to Geology*. Springer Textbooks in Earth Sciences, Geography and Environment, 2019.

Mcdannell, K. T., Issler, D. R., and Sullivan, P. B. O. :Radiation-enhanced fission track annealing revisited and consequences for apatite thermochronometry, *Geochim Cosmochim Ac.*, 252, 213–239, <https://doi.org/10.1016/j.gca.2019.03.006>, 2019.

Sandhu, A. S., Singh, L., Ramola, R. C., Singh, S., and Virk, H. S.: Annealing Kinetics of Heavy Ion Radiation Damage in Crystalline Minerals, *Nucl Instrum Methods.*, 122–124, 1990.

Shiple, N. K., and Fayon, A. K. Vanishing Act: Experiments on Fission Track Annealing in Monazite. AGU Fall Meeting Abstracts, 2006.

Shukoljukov, J. A., and Komarov, A. N.: Tracks of uranium fission in monazite (in Russian), *Bulletin of the Commission for the Determination of the Absolute Age of Geological Formations*, Moscow: Akad. Nau, USSR, pp. 20–26, 1970.

Tamer, M., and Ketcham, R.: Is Low-Temperature Fission-Track Annealing in Apatite a Thermally Controlled Process?, *Geochem Geophys Geosy*, 21(3), <https://doi.org/10.1029/2019GC008877>, 2020.

Tickyj, H., Hartmann, L. A., Vasconcellos, M. A. Z., Philipp, R. P., and Remus, M. V. D.: Electron microprobe dating of monazite substantiates ages of major geological events in the southern Brazilian shield, *J S Am Earth Sci.*, 16, 699–713, <https://doi.org/10.1016/j.jsames.2004.01.001>, 2004.

Ure, A.: Annealing characteristics of fission tracks in monazite: Application of a new method for performing thermal annealing experiments using implanted ²⁵²Cf fission fragment semi-tracks, BSc (Hons) thesis, School of Earth Sciences, The University of Melbourne, 2010.

839 [Wagner, G. A., and Van den Haute, P.: Fission-Track Dating \(2nd ed.\), Kluwer Academic](#)
840 [Publishers, Stuttgart, Germany, 1992.](#)
841 [Weise, C., van den Boogaart, K. G., Jonckheere, R., and Ratschbacher, L.: Annealing kinetics](#)
842 [of Kr-tracks in monazite: Implications for fission-track modelling, *Chem Geol.*, 260\(1–2\),](#)
843 [129–137, <https://doi.org/10.1016/j.chemgeo.2008.12.014>, 2009.](#)
844 [Yamada, R., Tagami, T., Nishimura, S., and Ito, H.: Annealing kinetics of fission tracks in](#)
845 [zircon: an experimental study, *Chem Geol.*, 122\(1–4\), 249–258,](#)
846 [https://doi.org/10.1016/0009-2541\(95\)00006-8, 1995.](#)

Deleted: Badr, M. J., Masoudi, F., Collins, A. S., & Cox, G. (2010). Dating of Precambrian Metasedimentary Rocks and Timing of their Metamorphism in the Soursat Metamorphic Complex (NW IRAN): Using LA – ICP- MS , U – Pb Dating of Zircon and Monazite. *Journal of Sciences*, 21(4), 311–319. [¶](#)
Belton, D. X. (2006). *The low-temperature thermochronology of cratonic terranes* School of Earth Sciences. The University of Melbourne. [¶](#)
Box, G. E. P., & Cox, D. R. (1964). An Analysis of Transformations. *Journal of the Royal Statistical Society. Series B (Methodological)*, 26(2), 211–252. [¶](#)
Cenki-Tok, B., Berger, A., & Gueydan, F. (2016). Formation and preservation of biotite - rich microdomains in high - temperature rocks from the Antananarivo Block , Madagascar. *International Journal of Earth Sciences*, 105(5), 1471–1483. <https://doi.org/10.1007/s00531-015-1265-0> [¶](#)
Clemens, J. D. (2018). Granitic magmas with I-type affinities , from mainly metasedimentary sources : the Harcourt batholith of southeastern Australia. *Contributions to Mineralogy and Petrology*, 173(11), 1–20. <https://doi.org/10.1007/s00410-018-1520-z> [¶](#)
Crowley, K. d., Cameron, M., & Schaefer, R. I. (1991). Experimental studies of annealing of etched fission tracks in fluorapatite. *Geochimica et Cosmochimica Acta*, 55(5), 1449–1465. [https://doi.org/10.1016/0016-7037\(91\)90320-5](https://doi.org/10.1016/0016-7037(91)90320-5) [¶](#)
Donelick, R. A., O’Sullivan, P. B., & Ketcham, R. A. (2005). Apatite Fission-Track Analysis. *Reviews in Mineralogy and Geochemistry*, 58(1), 49–94. <https://doi.org/10.2138/rmg.2005.58.3> [¶](#)
Donelick, Raymond A., Roden, M. K., Mooers, J. D., Carpenter, B. S., & Miller, D. S. (1990). Etchable length reduction of induced fission tracks in apatite at room temperature (~ 23°C): Crystallographic orientation effects and “initial” mean lengths. *International Journal of Radiation Applications and Instrumentation. Part, 17(3)*, 261–265. [https://doi.org/10.1016/1359-0189\(90\)90044-X](https://doi.org/10.1016/1359-0189(90)90044-X) [¶](#)
Fayon, A. K. (2011). Fission Track Dating of Monazite: Etching Efficiencies as a Function of U Content. In *GSA Annual Meeting* (p. 331). Minneapolis: Geological Society of America. [¶](#)
Fleischer, R. L., Price, P. B., & Walker, R. M. (1975). *Nuclear Tracks in Solids*. Berkeley: University of California Press. [¶](#)
Gleadow, A. J. . W., Raza, A., Kohn, B. P., & Spencer, S. A. S. (2004). The potential of monazite as a new low-temperature fission-track thermochronometer. Amsterdam: FT2004 10th International Conference on Fission Track Dating. [¶](#)
Gleadow, A. J. W., Gleadow, S. J., Frei, S., Kohlmann, F., & Kohn, B. P. (2009). Automated analytical techniques for fission track thermochronology. *Geochimica et Cosmochimica Acta Supplement*, 73, A441. [¶](#)
Gleadow, A., Kohn, B., & Seiler, C. (2019). The Future of Fission-Track Thermochronology. In M. Malusà & Fitzgerald P (Eds.), *Fission-Track Thermochronology and its Application to Geology* (pp. 77–92). Sptinger. [¶](#)
Green, P. F., Duddy, I. R., Gleadow, A. J. W., Tingate, P. R., & Laslett, G. M. (1985). Fission-track annealing in apatite: Track length measurements and the form of the Arrhenius plot. *Nuclear Tracks and Radiation Measurements (1982)*, 10(3), 323–328. [https://doi.org/10.1016/0735-245X\(85\)90121-8](https://doi.org/10.1016/0735-245X(85)90121-8) [¶](#)

... [1]

